DOI: 10.4408/IJEGE.2018-01.S-14

ENHANCED ONE-WAY COUPLED SWE-DE MODEL FOR FLOATING BODY TRANSPORT

Gabriella PETACCIA(*), Elisabetta PERSI(*), Stefano SIBILLA(*),
Pilar BRUFAU(**) & Pilar GARCÍA-NAVARRO(**)

(*)Università di Pavia - Dipartimento di Ingegneria Civile e Architettura - via Ferrata 3 - 27100 Pavia, Italy
(**)Universidad de Zaragoza -Departamento de Ciencia y Tecnología de Materiales y Fluidos - C/María de Luna, 3 - 50018 Zaragoza, España
Corresponding author: gabriella.petaccia@unipv.it

EXTENDED ABSTRACT

Il problema del trasporto di grandi detriti durante gli eventi di piena viene sempre più spesso affrontato facendo ricorso alla modellazione numerica. In letteratura esistono alcuni modelli bidimensionali, cinematici o dinamici, che consentono di stimare le traiettorie di tronchi trasportati dalla corrente, includendo a volte anche le interazioni tra i detriti stessi e con le sponde, e la formazione di ammassi in corrispondenza delle pile dei ponti. Gli aspetti che vanno presi in considerazione per lo sviluppo di questi modelli sono molteplici. Ad esempio, il metodo scelto per il calcolo del moto dei corpi rigidi galleggianti sulla superficie della corrente, le semplificazioni di forma dei detriti, la scelta del metodo numerico per il calcolo idraulico. Inoltre, decidere come accoppiare il calcolo idraulico e quello dello spostamento dei corpi rigidi, come far interagire i detriti tra loro e con le pareti, o come superare le difficoltà legate alle dimensioni variabili delle celle del dominio e degli elementi trasportati gioca un ruolo importante per il buon esito delle simulazioni.

In questo articolo si fa riferimento ad un modello di trasporto esistente, che accoppia la soluzione euleriana delle equazione delle acque basse in due dimensioni ad un metodo lagrangiano per il calcolo dinamico dello spostamento di elementi rigidi galleggianti. L'accoppiamento è di tipo *one-way*, ovvero le forze esercitate dal flusso sul corpo rigido sono utilizzate per calcolare accelerazione e spostamento, mentre l'effetto esercitato dai detriti sul flusso non viene considerato.

Un primo obiettivo dell'articolo è presentare le modifiche del modello che interessano la localizzazione del corpo rigido nella griglia di calcolo e l'assegnazione delle variabili idrauliche nei punti in cui vengono calcolate le forze. La versione originale del codice prevedeva l'utilizzo di un algoritmo di ricerca basato sulla sola valutazione della distanza tra il punto di interesse sul cilindro (che rappresenta un tronco galleggiante) e il centro delle celle di calcolo, individuando quella più vicina. Tale procedimento, valido per maglie cartesiane, introduce distorsioni nel calcolo della velocità relativa (velocità del flusso meno velocità del tronco) e, quindi, nella stima delle forze agenti sul tronco, se applicato a maglie triangolari non strutturate. E' stato quindi implementato un algoritmo aggiuntivo, che verifica che il punto di interesse cada esattamente nella cella individuata (*inclusion check*). In caso di esito negativo, l'algoritmo prende in considerazione le celle confinanti con la prima, fino a soddisfare il criterio di inclusione.

Per superare il limite legato alla dimensione reciproca di celle e corpo rigido, che portava alla assegnazione di un unico valore di velocità per tutto il cilindro nel caso in cui la cella avesse dimensioni maggiori dello stesso, è stato implementato un procedimento di doppia interpolazione. I valori calcolati a centro cella vengono utilizzati per calcolare i valori ai nodi e, da questi, si interpolano i valori in corrispondenza dei punti di interesse sul cilindro. In questo modo, anche se il cilindro è incluso in un'unica cella, è possibile stimare la distribuzione di velocità lungo la sua massima dimensione.

Nella seconda parte dell'articolo si fa riferimento al metodo di rappresentazione degli ostacoli presenti all'intero del canale. Due distinte metodologie vengono confrontate: l'area occupata dall'ostacolo viene esclusa dalla griglia di calcolo e i suoi bordi diventano pareti del dominio; l'ostacolo viene rappresentato con celle ad elevata resistenza idraulica, calibrando il coefficiente di Manning in modo che il campo di moto risulti conforme ai valori precedentemente misurati. L'effetto di questi due metodi viene valutato sia da un punto di vista idraulico, confrontando il campo di moto, sia in riferimento al trasporto di detriti. I risultati evidenziano che, in generale, aumentando la resistenza idraulica vengono ridotti i picchi (positivi e negativi) di velocità, fattore che contribuisce a migliorare l'accuratezza della simulazione del moto di corpi rigidi galleggianti.

Le differenze riscontrate tra i due metodi, però, vengono meno quando la traiettoria del cilindro è disturbata da fattori esterni, quali urti con le parti, che alterano l'orientamento del corpo e allontanano in modo netto l'esito della simulazione dal risultato atteso. Tuttavia, una analisi di dettaglio riguardante il metodo scelto per la modellazione degli urti va oltre lo scopo di questo contributo.

In conclusione, i miglioramenti introdotti nella ricerca delle celle e nella interpolazione dei valori dal flusso al corpo rigido, oltre alla analisi dell'effetto delle due metodologie di rappresentazione degli ostacoli, hanno permesso di evidenziare il buon funzionamento del modello di trasporto dei detriti, che resta, però, fortemente influenzato dai fenomeni casuali (urti, turbolenza).

ABSTRACT

Modelling the transport of floating bodies during floods is a topic that must be considered when dealing with flood risk, but many open issues still exist regarding its implementation. The paper presents an enhanced one-way coupled SWE-DE (Shallow Water Equations-Discrete Element) model, focusing on to the algorithm for the rigid body localization and on the interpolation of the flow velocity distribution along the body. The proposed algorithm leads to a smoother variation of the hydrodynamic coefficients. Moreover, the higher accuracy in assigning the flow velocity, needed to compute the forces on the bodies, reduces the dependence on the relative size of the cells and objects. A laboratory case has been used to validate the model in which some rectangular obstacles are present. Obstacles were represented by modelling them as solid walls or by increasing the Manning roughness coefficient. The influence of the two schematizations on the flow field and on the transport of a floating cylinder is evaluated. On overall, varying the obstacle roughness coefficient yield trajectories closer to the observed ones, although external factors, such as the effect of cylinder orientation and of collisions with side walls, may occasionally alter the outcome of the simulation.

***Keywords**: floating large bodies, wood transport, rigid body transport, shallow water, obstacle numerical modelling, roughness*

INTRODUCTION

Modelling wood transport is a strategy that is increasingly taken into consideration when dealing with flood risk estimation (e.g. Ruiz-Villanueva *et alii*, 2014a). The motion of floating bodies on the water surface can be considered as the interaction of a continuous phase (water) and a discontinuous one (debris), but how to tackle the presence of floating discrete elements in a flow is still an open issue. In some cases, the 2D displacement of a volume of wood, computed by considering the wood budgeting, is performed (Mazzorana *et alii*, 2011), disregarding the physical response of the single floating object.

Another possibility is the use of hybrid 2D methods, characterized by the coupling of two different techniques for the solution of the two phases. The flow velocity may be computed by solving the full Navier-Stokes equations with the Volume of Fluid method (e.g. Fekken, 1975), or, more frequently, by the numerical solution of the Shallow Water Equations (SWE) with a finite volume code. For the discontinuous phase, Ruiz-Villanueva *et alii* (2014b) proposed a kinematic approach, in which the flow velocity and vorticity are simply assigned to the logs as linear and angular velocity. On the other hand, dynamic methods can be applied (Alonso, 2004; Stockstill *et alii*, 2009), in which the computation of the hydrodynamic forces exerted by the flow on the rigid body is required, so that the body acceleration can be calculated.

In this framework, Persi *et alii* (2018) proposed a 2D method based on the one-way coupling of the Eulerian solution of the SWE and the Lagrangian Discrete Element (DE) dynamic description of the body transport. The translation is computed by adapting the Basset-Boussinesque-Oseen equation (e.g. Maxey & Riley, 1983) to the case of large floating bodies, while rotation is calculated following the strategy proposed by Mandø & Rosendahl (2010). In addition, the cylinders (which represent wooden logs) are divided in 4 segments, to take into account the approximated distribution of the flow velocity on elongated elements. The forces are thus computed for each subsection, by considering the velocity (and acceleration) of the flow in the cell where the centre of mass of each sub-segment is found, as well as the body velocity in that point.

The application of the model to the case of cylinders floating on the water surface in a laboratory channel (Ruiz-Villanueva *et alii,* 2014b) highlighted the sensitivity of the model to (i) the correct localization of the cell and to the flow velocity assignment in the four computational points (segments representing the logs), in order to compute the hydrodynamic forces, and (ii) the influence of the flow field, and, in particular, of the representation of the inline or side obstacles.

Both factors affect the outcome of the simulations. For this reason, the localization procedure of the segments was improved with respect to the first version proposed in Persi *et alii* (2018), and different obstacle representations were tested.

LOCATION ALGORITHM AND ASSIGNMENT OF THE VELOCITY TO THE RIGID BODIES

In order to simulate rigid body motion, the hydrodynamic force due to the velocity distribution along the cylinder (floating body) needs to be computed. As hydrodynamic coefficients are usually obtained in uniform flow conditions, the effect of the velocity variation along the major axis of the body is approximated by dividing it into four segments. Velocities, and hence forces, are therefore evaluated in four points, which are the centres of mass of these four segments of length L/4. At each time, the position of the body centre of mass, its dimensions and orientation are needed, as well as its linear and angular velocities. Then, the coordinates of the centres of the four body segments are calculated by considering their distance from the centre of mass and the body orientation.

At the moment of computing the forces acting on each segment, it is necessary to identify in which mesh cell each point is located. Two typical cases can be considered, depending on the size of the cells: when the cell average size is smaller than the body main dimension (Fig. 1a), and when the cells are large enough to include the body in a single element (Fig. 1b).

Even if these configurations involve a different number of cells, it is essential to assign in both cases to each point the correct

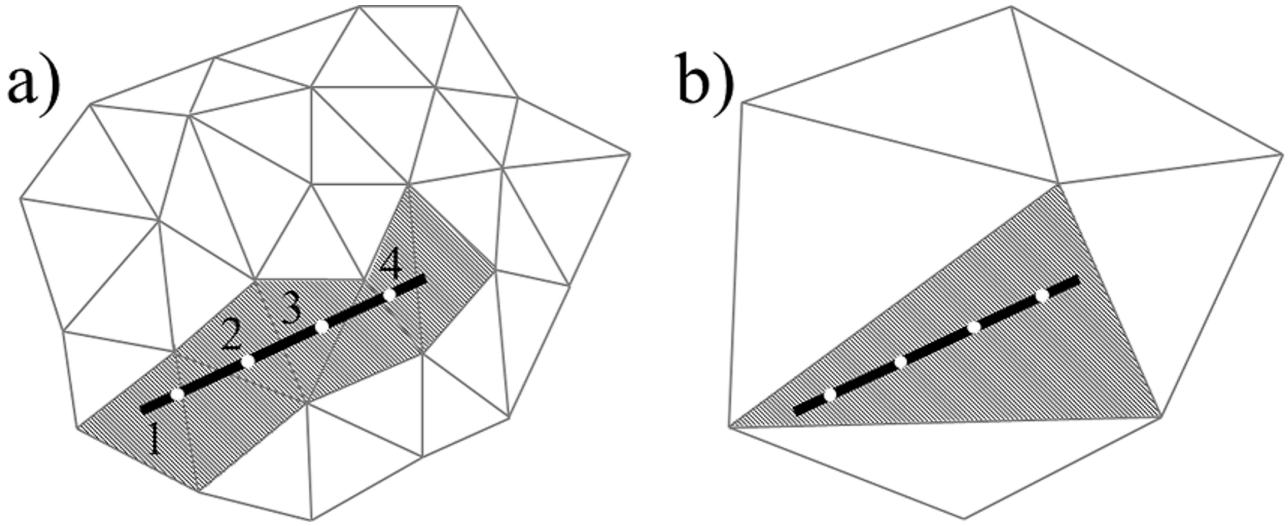

Fig. 1 - Cells and rigid body dimensions. The black solid line represents the rigid body and the white points are the centres of the four segments; a) the main dimension of the rigid body is larger than the cell average size; b) the main dimension of the rigid body is smaller than the cell average size

flow velocity, independently from the cell size. This flow velocity must be interpolated from the available values at the cell centres: as this interpolated value determines the forces acting on each body segment, the interpolation method must guarantee a smooth variation when the segment centre moves within a cell or from a cell to a neighbouring one, in order to avoid numerical discontinuities in the hydrodynamic forces acting on the body.

Cell location algorithm

As a first attempt, the cell in which a point resides may be identified as the cell whose centre of mass is nearest to the point (nearest neighbour criterion). This basic strategy is appropriate in the case of a structured Cartesian mesh but may result unsuccessful in a triangular mesh, if the cells are skewed or if their size varies sharply. Fig. 2 shows an example in which the nearest cell is not the cell in which the point is located. Such a mismatch, during the simulation, may result in abrupt variations of the flow velocities assigned to the computational point and has an impact on the computation of the relative velocity and angle, as well as of the hydrodynamic coefficients (which depend on the relative angle).

Different point location methods can be found in the literature (e.g. Kirkpatrick, 1983, Edahiro *et alii*, 1984, Preparata, 1990, Mücke *et alii*, 1999). Here, a new method, inspired by the one proposed by Soukal *et alii* (2011), has been implemented and integrated in the numerical procedure . The main idea behind the method by Soukal *et alii* (2011) is the use of the rotation matrix to align on an oriented horizontal line one vertex of the mesh, belonging to a randomly selected cell, and the point of interest. Then, the exact triangular cell is identified through the Remembering Stochastic Walk algorithm by Devillers *et alii* (2001).

The method proposed in this paper takes advantage of the fact

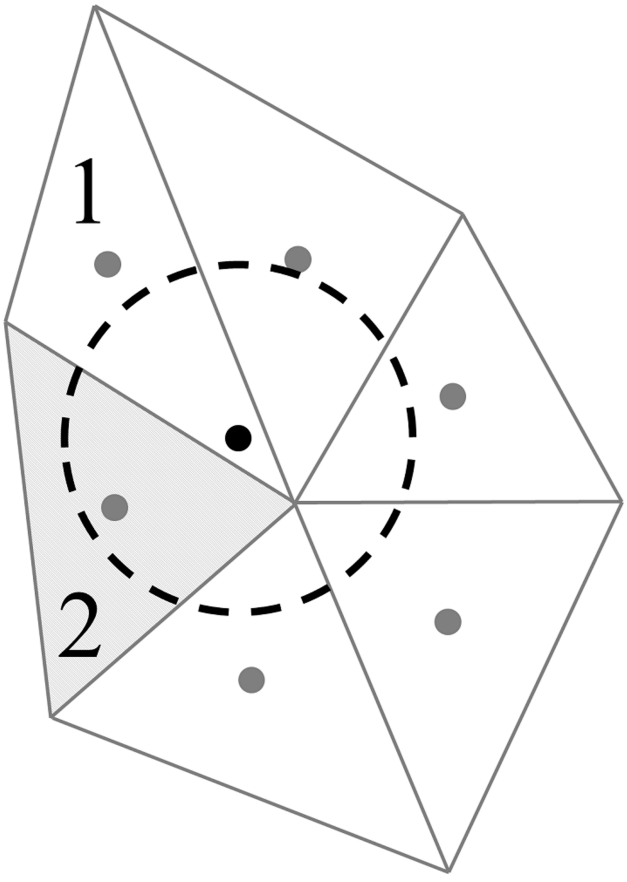

Fig. 2 - Failure of the nearest neighbour criterion: the black point is located in cell 1, but the nearest cell centre is that of cell 2 (grey lines). Dashed black lines approximates the minimum distance between the point and the cells' centres

that the cell found with the nearest neighbour criterion is already very near to the correct one, so that only a short walk is required. Starting from that cell, the idea is to check if the point is inside it or not. A side of the triangle is selected and the coefficients of the rotation matrix are computed as in Eqs. 1 and 2.

$$k\cos(\beta) = x(1) - x(2) \quad (1)$$

$$k\sin(\beta) = y(1) - y(2) \quad (2)$$

where β is the angle between that triangle side and an horizontal line, x and y are the coordinates of the two vertices of that side, whose length is k.

The y coordinate of one of the vertex (alternatively 1 or 2) is transformed to y', and set as the reference horizontal axis. Then, the y coordinates of the point of interest p and of the vertex not already used to compute the rotation matrix (vertex 3, to follow the numbers of this example) are transformed, too, and their distance with respect to the new horizontal axis is computed as shown in Eqs. 3 and 4:

$$y'_p = -x_p k\sin(\beta) + y_p k\cos(\beta); \quad d_p = y'_p - y'(1) \quad (3)$$

$$y'(3) = -x(3)k\sin(\beta) + y(3)k\cos(\beta); \quad d_2 = y'(1) - y'(1) \quad (4)$$

where vertex 1 is selected as for the origin of the horizontal axis.

If the product of the distances d_p and d_3 is greater or equal to zero, the point of interest is on the same side of the free vertex 3, and the logical flag

$$f_{12} = (d_p d_2 > 0) = TRUE \quad (5)$$

for that side. The procedure is repeated for each side of the triangle, and if the other flags f_{23} and f_{31} are also *TRUE*, the point is actually located in that cell.

On the contrary, if one of the logical flags is *FALSE*, the point is certainly not located in that cell: the procedure moves then to the triangle adjacent to that side and all the above mentioned steps are repeated.

This algorithm, named inclusion check algorithm, is quite simple, requires few operations for each repetition and only three recurrences if the cell found with the nearest neighbour criterion is already the correct one. In the enhanced model it is applied to each of the four computational points (the four centres of the segments) when the mesh is triangular, and regardless of the shape of the triangular cell, it is able to locate the point exactly.

Velocity assignment to the four computational points

Once that the correct cell is located, the flow velocity has to be assigned to the points which represent the rigid body. The finite volume method for the solution of the SWE provides the water depth and velocity at each cell centre. A zero-th order interpolation, assigning to each point the values of the cell in which they reside, may result inappropriate: in the configuration of Fig. 1a, if the values of cells from 1 to 4 were directly assigned to the four points of the rigid body, an approximation of the velocity distribution along the body main dimension would be anyway obtained, while in the configuration of Fig. 1b, a single value would be assigned to all of the four points, totally missing any velocity gradient.

With the objective of maintaining the effectiveness of the subdivision of rigid bodies in segments, the interpolation of the velocity from the cell centres is required. Furthermore, to ensure the success of the interpolation for any location of the points, two steps are performed: firstly, the nodal values are interpolated from the values at the cell centres (Fig. 3a) and then the value for the considered point is interpolated from the nodal quantities (Fig. 3b). It is worth highlighting that the interpolation procedure has to be performed for each of the centres of the body segments.

A general scheme of interpolation valid for a two-dimensional domain is:

$$U(x) = \sum_{i=1}^{n} \varphi_i(x)\, Ui(x) \quad (6)$$

where $U(x)$ is the value of the scalar function (such as one of the components of flow velocity, or the water level) at the point of interest, $\phi_{i(x)}$ is the shape function for the interpolation node i and $Ui(x)$ is the known scalar function value at the interpolation node.

To perform the interpolation from centred values to nodal values (Fig. 3a), the number of cells n sharing the same vertex is a priori unknown. The shape functions have thus to be valid for any irregular convex n-gons. The generalization to convex irregular n-gons of the Wachspress shape functions proposed by Meyer *et alii* (2002) and by Sukumar & Tabarrei (2004) is thus implemented. The procedure is repeated for each vertex of the selected cell, so that the flow velocity in this case, as well as any other quantity of interest, is obtained at each node.

The velocities at the mesh nodes are then used to estimate the flow velocity for each body segment . In the case of a triangular mesh, the piecewise polynomial interpolation of degree I is implemented (e.g. Hirsch, 1991).

This two-step interpolation mantains a detailed description of the velocity distribution on the body. However, several recurrences are needed, first of all to obtain the values of the flow variables at the vertices of each cell of interest – where the computation points are located – and then to interpolate the vertex values on the computational points. For this reason, the interpolation procedure is performed only for the cells where the computational points are located.

OBSTACLE REPRESENTATION

The effect of the obstacle modelling on the flow computation, and thus on the rigid body motion, is analysed by comparing results obtained with the same geometry but with different strategies to represent the side obstacles. Two different methods are tested: (i) obstacles are excluded from the mesh (e.g. Aronica & Lanza 2005, Bazin *et alii*, 2016) or (ii) they are represented as areas with higher roughness coefficient (e.g. Soares-Frazão *et alii*, 2008; Petaccia *et alii*, 2010). Figure 4 shows a detail of the mesh for the abovementioned approaches. In Fig.

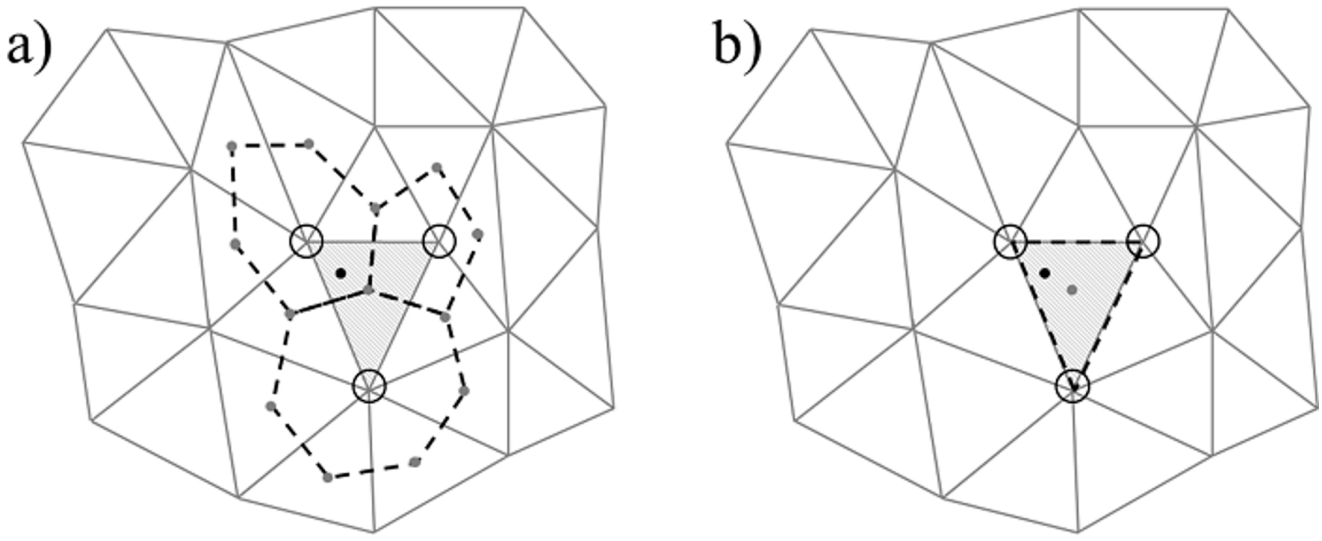

Fig. 3 - a) First step of interpolation: from cell values to vertex values; b) second step of interpolation: from vertex values to point values

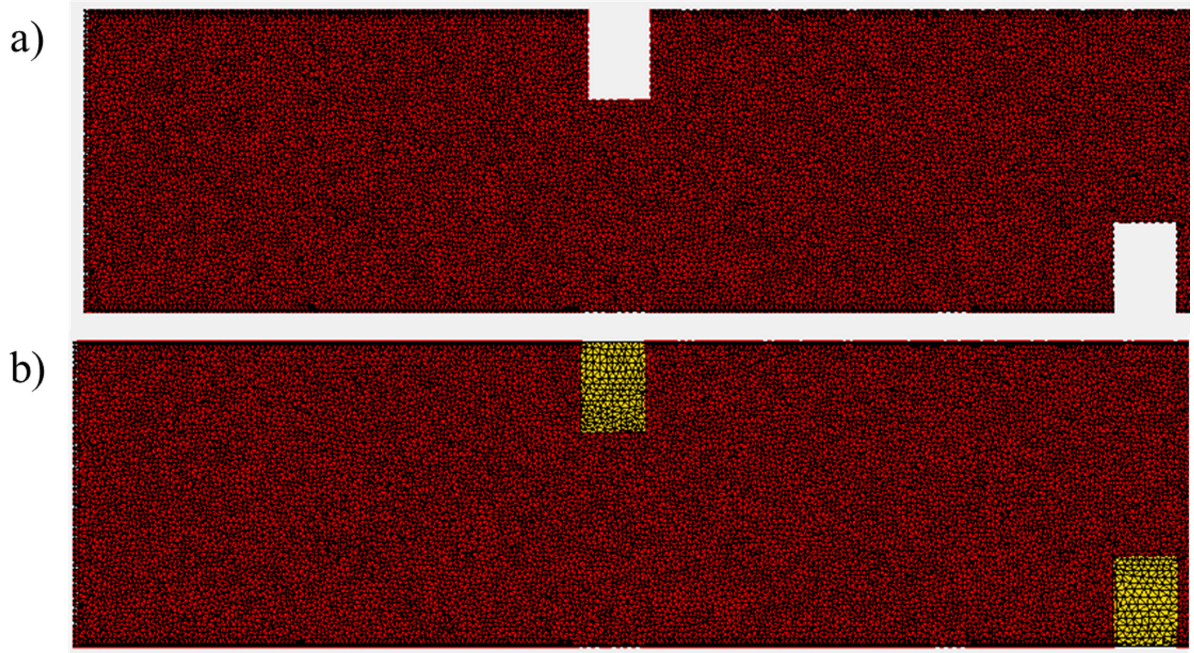

Fig. 4 - Detail of the computational domain with the different methods of obstacles representation: a) obstacles excluded from the mesh, with walls; b) obstacles with different Manning coefficient (yellow colour refers to different roughness)

4a the obstacles are excluded from the mesh, which means that the flow and the cylinders encounter a solid wall where complete reflection is considered.

In the second case (Fig. 4b) the obstacles are included in the mesh, and their effect is modelled by locally varying the Manning coefficient (different colours refer to different roughness coefficient values).

The hydraulic simulation is performed with the finite volume code ORSA2D (Petaccia *et alii*, 2010, Petaccia *et alii,* 2016), which implements a Roe's Riemann solver, 1st-order accurate in time and space (Roe, 1981), applying an upwind discretization to the bottom slope source term (Bermúdez *et alii*, 1998), while the friction slope is evaluated in a semi-implicit way (Costabile *et alii*, 2015). The version of the Harten-Hyman entropy fix is used (Toro, 2009) to avoid the presence of non-physical results due to the linearization procedure.

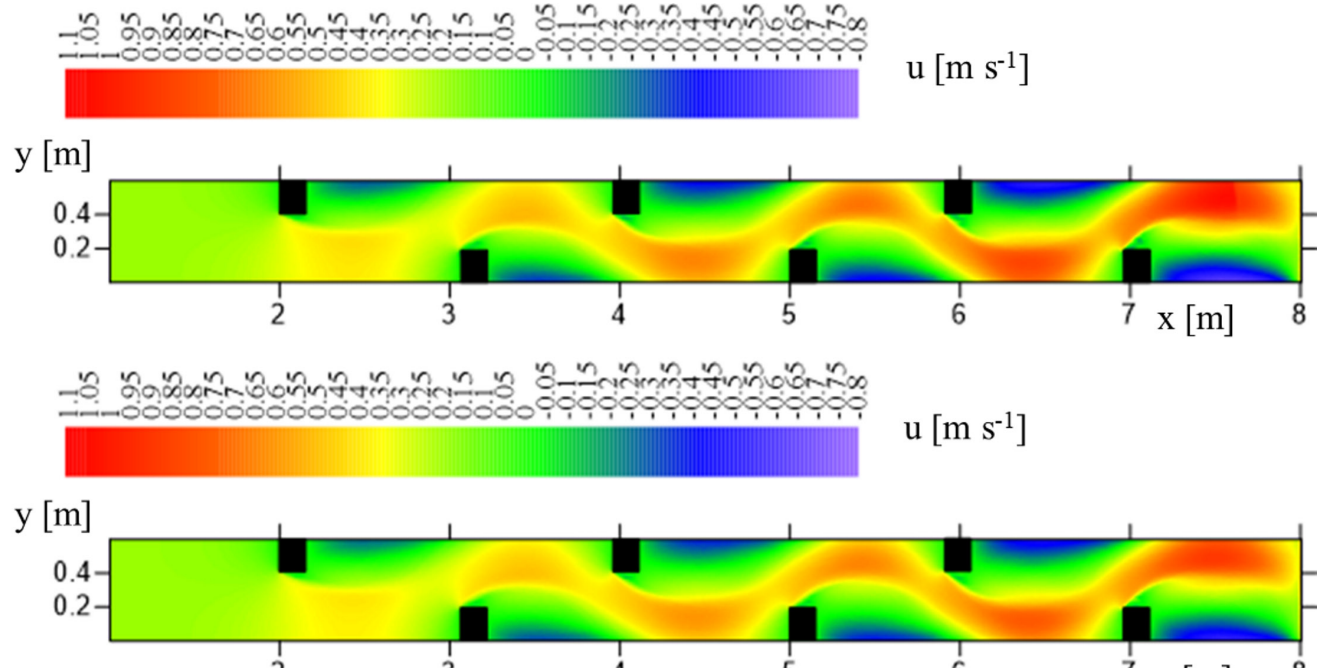

Fig. 5 - Streamwise component of velocity, u [m s-1], for the two obstacle representations: walls (up), roughness (down)

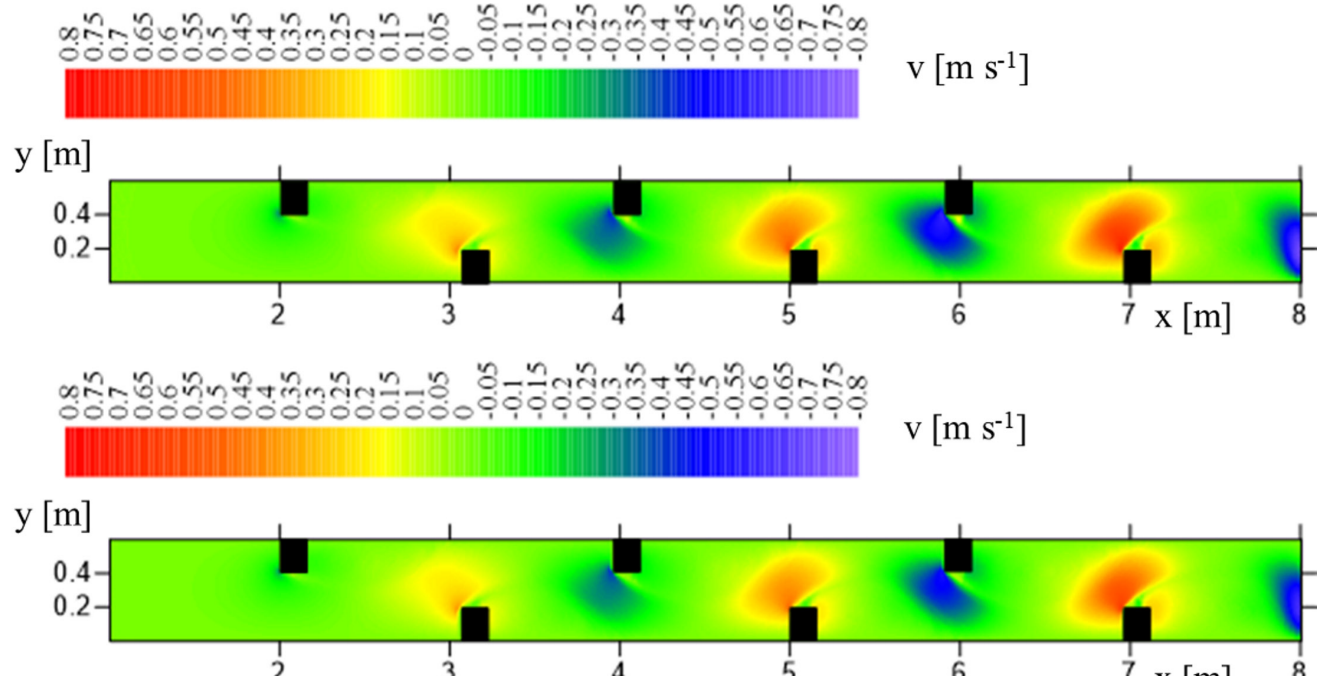

Fig. 6 - Transversal component of velocity, v [m s-1], for the two obstacle representations: walls (up), roughness (down)

The selected case study for the comparison of the flow field is a laboratory flume (7.00 m long, 0.60 m wide, with a constant discharge of 18 l s^{-1}) with six rectangular side obstacles with dimensions 0.13x0.18 m; the case study was provided by Ruiz-Villanueva *et alii* (2014b). The simulation is performed on an unstructured triangular mesh (nearly 85000 elements) with a Manning coefficient equal to 0.01 s $m^{-1/3}$ for the channel bottom, and to 10 s $m^{-1/3}$ for the obstacles when method (ii) is applied.

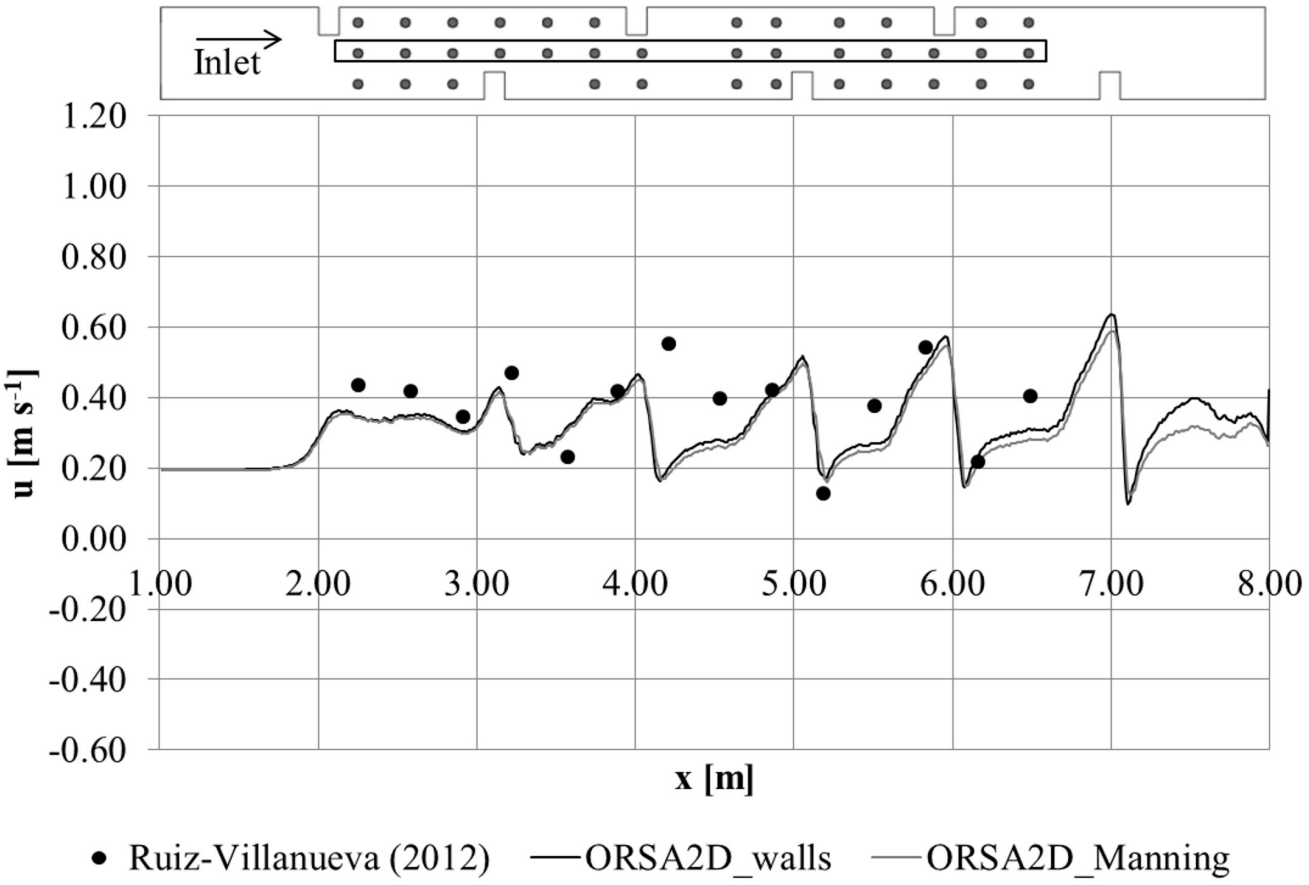

Fig. 7 - Comparison of measured and computed axial component of the velocity in a longitudinal profile along the channel axis. The sketch of the channel above the graph shows the points of measure

These values are calibrated in order to provide a good reproduction of the velocities measured in the channel.

Figs. 5 and 6 show the contour maps with the streamwise and transversal velocity components, which are shown separately to highlight the characteristics of each obstacle representation.

As regards the streamwise component of velocity, the representation with walls yields higher values of minimum and maximum velocity (1.06 m s^{-1} and -0.64 m s^{-1}), while the method with a higher Manning coefficient presents a smoother transition of velocity between the obstacles and in the final part, and slightly lower peak values (0.9 m s^{-1} and -0.58 m s^{-1}).

Also for the transversal velocity component, the first method reaches higher values (0.71 m s^{-1} and -0.71 m s^{-1}) than those obtained with the Manning coefficient (0.64 m s^{-1} and -0.67 m s^{-1}). As for the streamwise component, the latter shows a smoother transition among the main channel and the recirculation areas.

To assess how the obstacle representation influences the flow computation, the simulated velocities are compared with the ones measured by Ruiz-Villanueva *et alii* (2014b). Figures 7, 8 and 9 show the comparison of the measured and simulated velocity (with the two methods used to represent the obstacles) at the channel axis. The location of the points of measure is also reported.

The velocity comparison shows that the effect of the different strategies for obstacle representation is more evident on the left and on the right side, than in the mid channel. In particular, the negative values of streamwise velocity (which corresponds to areas of recirculation downstream the side obstacles) are smaller when the simulation is performed with the higher Manning coefficient.

The correlation coefficients reported in Tab. 1 highlight that, in general, the computation of velocity along the centreline is less accurate for both implemented methods, while on the right and left sides the representation of the obstacles with side walls provides slightly better results.

On overall, the velocity prediction is satisfactory, since it provides good correlation with the available measures.

Method	R^2 – centreline	R^2 – right side	R^2 – left side
Walls	0.829	0.986	0.990
Manning	0.843	0.978	0.986

Tab. 1 - Comparison of the correlation coefficient for the two obstacle representations and for the three groups of measurement

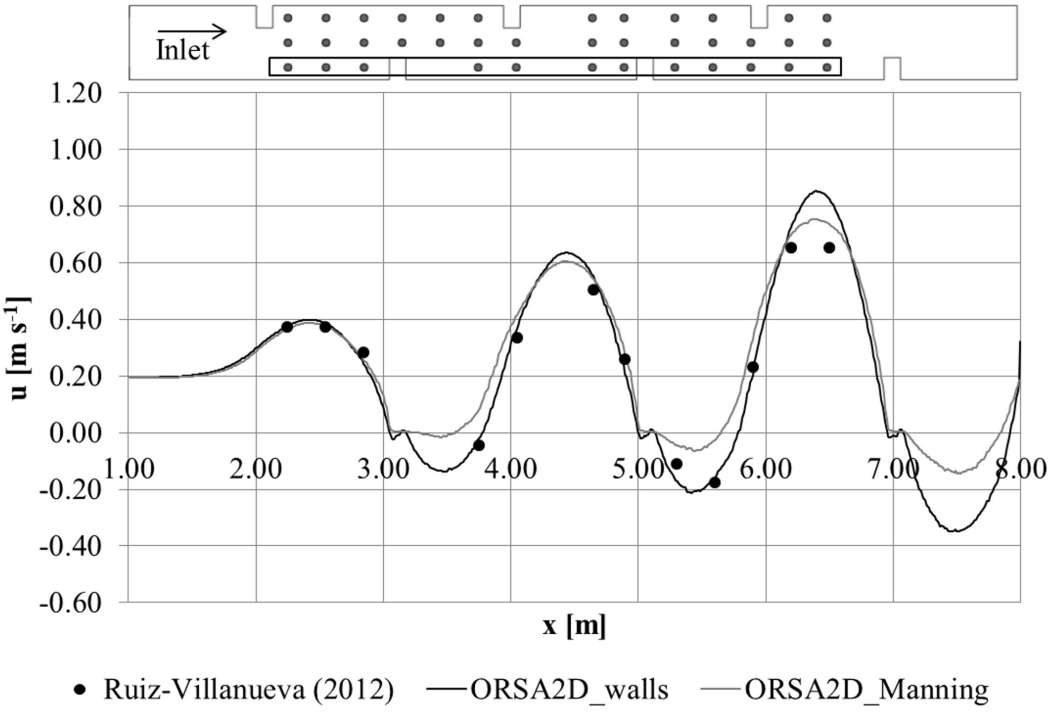

Fig. 8 - Comparison of measured and computed streamwise component of the velocity in the right hand side of the channel. The sketch of the channel above the graph shows the points of measure

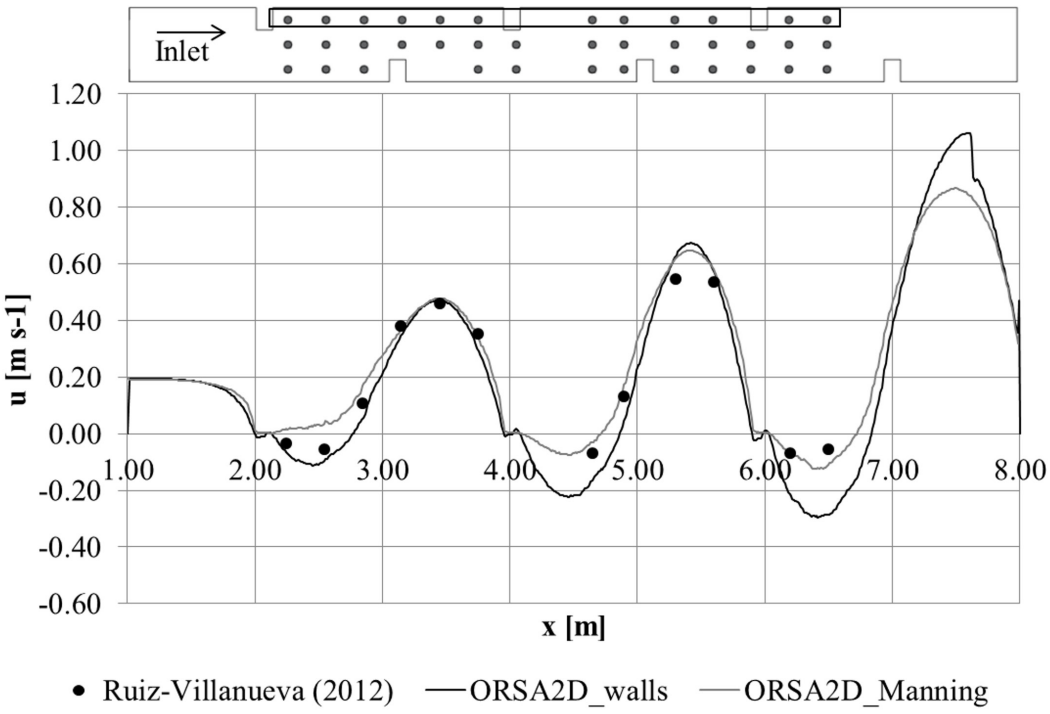

Fig. 9 - Comparison of measured and computed streamwise component of the velocity in the left hand side of the channel. The sketch of the channel above the graph shows the points of measure

EFFECT ON WOOD TRANSPORT

Focusing on the effect of the new implemented algorithm, Fig. 10 shows an example of how the drag coefficient of the cylindrical sample varies within a selected time interval when the nearest cell is found by applying either the nearest neighbour criterion or with the inclusion check algorithm. The drag coefficient, in the model by Persi *et alii* (2018), is a function of the relative velocity of the log with respect to the flow, thus depending on the correct identification of the cell for each computational point. If the cell is found with the nearest neighbour criterion, the value of the drag coefficient oscillates strongly, because of the abrupt variation of the relative angle when the cell is not correctly identified. The reduction of the computed coefficient oscillations when the inclusion check algorithm is included in the model is evident.

The variations observed in the flow field due to the different representation of the obstacles may affect the outcome of the simulation of wood transport. To verify the extent of such alterations, the simulation of wood transport in a laboratory flume is performed. The abovementioned methods for obstacle representation are applied to two geometries which differ for the dimension of the side obstacles. The first case is the one already introduced for the comparison of velocity, with six side obstacles of dimensions 0.13x0.18 m, from now on named Geometry 1, while the second, Geometry 2, presents six side obstacles which measure 0.13x0.27 m and occupy nearly a half of the channel. Both cases are from Ruiz-Villanueva *et alii* (2014b).

The wooden sample (density 720 kg m^{-3}) employed for Geometry 1 has length 0.20 m and diameter 0.018 m while for Geometry 2 it has the same length and a diameter of 0.008 m.

In Figs. 11 and 12 the trajectories obtained for Geometry 1 and Geometry 2 are shown, comparing in each one the two different obstacle representation methods. In both cases, the initial position of the sample is set equal to the first position recorded by Ruiz-Villanueva *et alii* (2014b), and the cylinder is set perpendicular to the flow direction (i.e. aligned with the y axis).

For Geometry 1, the trajectories computed with ORSA2D_DEM (which is the model described in Persi *et alii* (2018), updated with the location algorithm presented here and the velocity assignment procedure described) are similar and follow quite well the measurements. Downstream of the third obstacle, the simulation performed with obstacles represented by higher Manning coefficients (dashed line in Fig. 11) is nearer to the experimental observations. The correlation coefficients, shown in Tab. 2, confirm that the simulation performed with higher values of the Manning coefficients provides better results, especially in coordinate y.

As regards Geometry 2, the presence of larger obstacles leads to a sharper trajectory, with the cylinder floating near the walls and the obstacles, being involved also in collisions with the side

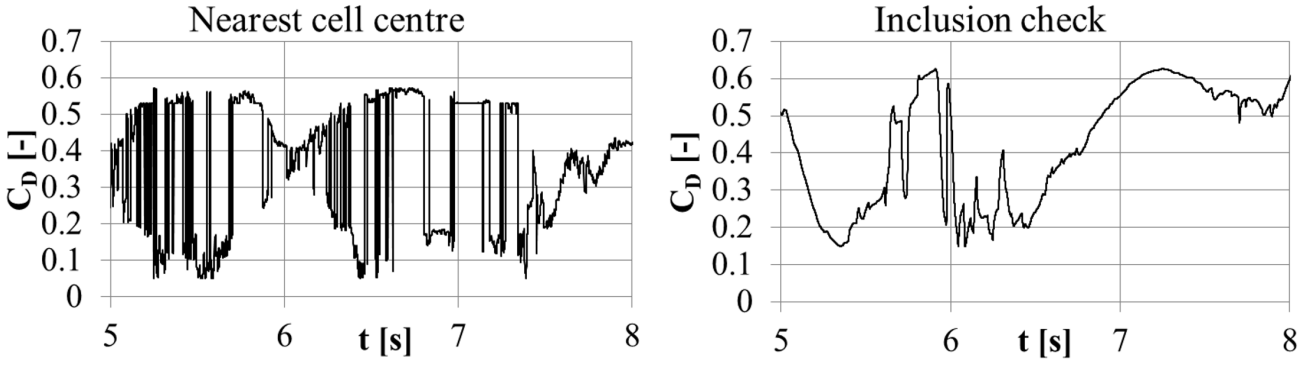

Fig. 10 - Trend of the drag coefficient with the nearest cell centre (left) and the inclusion check algorithm (right)

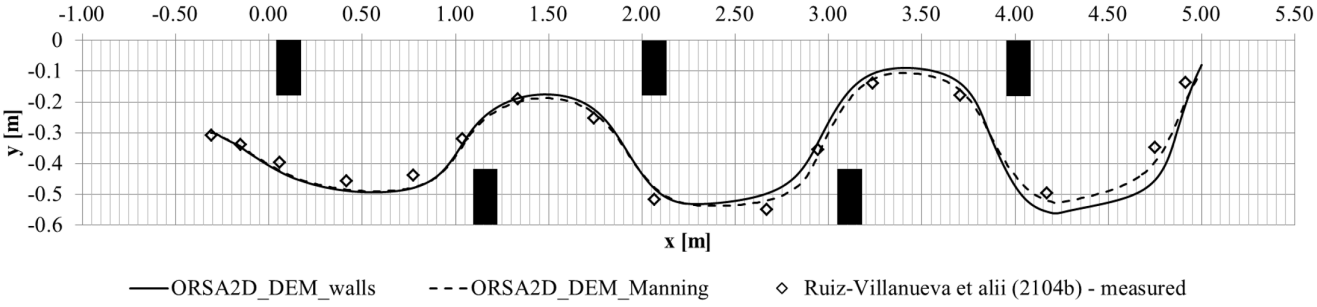

Fig. 11 - Comparison of the cylindrical sample trajectory with the different obstacles representation for Geometry 1: black line for walls, dashed black line for higher Manning coefficient. The results measured by Ruiz-Villanueva et alii (2014b) are shown by empty diamonds. Black rectangles represent the obstacles

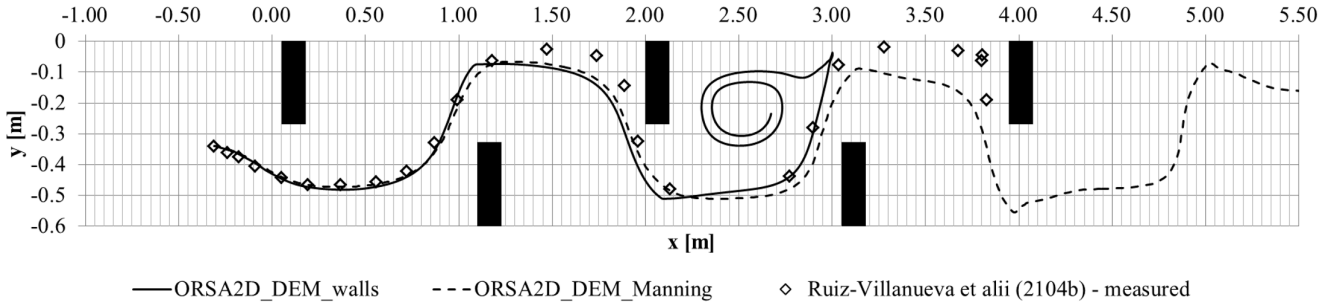

Fig. 12 - Comparison of the cylindrical sample trajectory with the different obstacles representation for Geometry 2: black line for walls, dashed black line for higher Manning coefficient. The results measured by Ruiz-Villanueva et alii (2014b) are shown by empty diamonds. Black rectangles represent the obstacles

of the channel. In this case, the trajectories differ from the expected one, especially when collision occurs.

Collisions can be detected by the abrupt variation of the trajectory, as can be seen, for example, around $x = 1.10$ *m* for the simulation performed with obstacles as walls (black line in Fig. 12). After each collision, the simulated trajectory becomes different from the expected result.

For the simulation performed with obstacles as walls, the cylinder collides three times with the walls. After the last collision, it is recirculated downstream the third obstacle, totally missing the measured trajectory.

Collisions can be observed also when the obstacles are represented by a higher Manning coefficient (dashed line in Fig. 12), although no recirculation occurs. In this case, the main difference with respect to the measured trajectory is the path of the cylinder upstream of the third and fifth obstacles. In the experiments, the cylinder floats very near the flume walls, while in the simulation it remains a few centimetres apart, probably due to the interaction with the rigid boundaries. The correlation coefficients are computed also in this case (Tab. 3), showing that the two methods provide similar results.

Note that the slightly higher correlation coefficient for coordinate y obtained with the wall representations (0.756) is due to the fact that, with this configuration, the cylinder goes nearer to the left side wall. Figure 13 shows the y positioning of the centre of mass of the cylinder at different times, for the two obstacle representation methods. In both cases the y displacement is delayed with respect to the observed results, but for the case with walls the positions are nearer to the expected ones, although the cylinder is recirculating. The higher value shown in Tab. 3 is thus related to the vicinity to the left side wall around $t = 11$ *s* and not to the accuracy in the overall trajectory simulation.

CONCLUSIONS

This paper discusses some of the features which need to be addressed when implementing an Eulerian-Lagrangian model that simulates the transport of floating bodies in a flow. The computation of the motion of rigid bodies requires actually to consider carefully several aspects. Apart from the choice of the transport model, which is not the main focus of the present paper, one should pay attention to the correct localization of the cells where the body is found and to the cell/body relative dimensions. The inclusion check algorithm here proposed removes the localization mistakes. Since the identified cell is exact, the unpredictable variations in the relative velocity are avoided, leading to a more precise evaluation of the hydrodynamic coefficients and, consequently, of the forces on the body. Furthermore, with the two-step interpolation procedure the distribution of the flow velocity on elongated bodies can

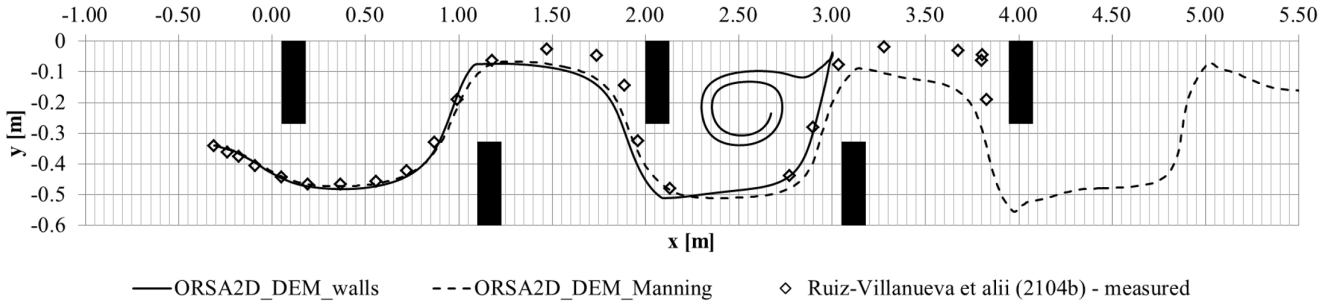

Fig. 13 - Comparison of the y positioning of the centre of mass of the cylindrical sample against time, with the different obstacles representation for Geometry 2: black line for walls, dashed black line for higher Manning coefficient. The results measured by Ruiz-Villanueva et alii (2014b) are shown by empty diamonds

Method	R^2 *x*	R^2 *y*
Walls	0.999	0.682
Manning	0.999	0.929

Tab. 2 - Comparison of the correlation coefficient computed with reference to the x and y coordinates for Geometry 1 for the two obstacle representation models

Method	R^2 *x*	R^2 *y*
Walls	0.994	0.756
Manning	0.995	0.733

Tab. 3 - Comparison of the correlation coefficient computed with reference to the x and y coordinates for Geometry 2 for the two obstacle representation models

be estimated independently from the cell/body size ratio. This is a crucial achievement, because the correct estimation of the flow velocity is fundamental for the simulation of rigid body motion, since the force computation depends strictly on this value.

The inclusion of obstacles in the domain can be faced with different techniques, so it is important to verify which method provides the best results, both in terms of flow estimation and of floating body motion. Two approaches are tested in this paper: in the first case, obstacles are excluded from the mesh, while, in the second, they are considered as areas with high hydraulic resistance, which translates in an extremely high value of the Manning coefficient. In particular, for the considered case, the Manning coefficient implemented to obtain the correct simulation of the flow around the obstacles is one-thousand times higher than the base value assigned to the flume bottom.

By comparing the flow fields obtained with these two methods, it appears that by increasing the Manning coefficient the maximum and minimum velocity present lower absolute values. On overall, however, by comparing the simulated velocity with the measured one for a flume experiment, the two methods result nearly equivalent.

On the contrary, the effect on the transport of floating bodies is not the same. Despite the small differences in the flow field, the reduction of the peaks observed when the obstacles are represented by higher Manning coefficient has a positive impact on the body trajectory, especially when the transport is not affected by external factors. It is worth highlighting, however, that such a result is obtained by calibrating the value of the obstacle Manning coefficient based on existing flow measurements. This procedure is more difficult to perform in field condition.

The prediction of the body trajectory becomes more difficult when particular circumstances, i.e. collisions with walls, occur. ORSA2D_DEM accounts for collisions, but the restitution coefficient has been only qualitatively calibrated (set equal to 0.1, thus obtaining nearly inelastic collisions with walls) and its variation may affect the outcome of the simulation. Furthermore, if subsequent collisions happen (as in Fig. 12), the trajectory is strongly modified and provides results departing from the expected ones, e.g. cylinder trapped in the recirculation downstream the obstacle. The body orientation, here not examined due to the lack of experimental data, contributes to the different interaction with walls and to the progress of the body trajectory, too.

On overall, the improvement implemented and the detailed analysis of the obstacle representation helps in enhancing the model of floating bodies transport. The simulations shown in the paper highlight, however, that some other aspects deserve additional work, such as the calibration of the collision model and the in-depth analysis of the computation of body rotation.

ACKNOWLEDGMENTS

The authors thank Dr. Virginia Ruiz-Villanueva for sharing data on flow velocity and on wood transport.

REFERENCES

Alonso C.V. (2004) - *Transport mechanics of stream-borne logs.* In: Sean J.B. & Andrew S. (Eds.) - *Riparian vegetation and fluvial geomorphology.* Water Science and Applications, **59-69**, American Geophysical Union, Washington, D.C.

Aronica G. & Lanza L. (2005) - *Drainage efficiency in urban environment.* Hydrol Process, **19** (5): 1105-1119.

Bazin P.H., Mignot E. & Paquier A. (2017) - *Computing flooding of crossroads with obstacles using a 2D numerical model.* J Hydraul Res, **55** (1): 72-84.

Bermúdez A., Dervieux A., Desideri J.A. &Vázquez M.E. (1998) - *Upwind schemes for the two dimensional shallow water equations with variable depth using unstructured meshes.* Comput Method Appl M, **155** (1-2): 49-72.

Costabile P., Macchione F., Natale L. & Petaccia G. (2015) - *Flood mapping using LIDAR DEM. Limitations of the 1-D modeling highlighted by the 2-D approach.* Nat Hazards, **77** (2): 181-204.

Devillers O., Pion S. & Teillaud M. (2001) - *Walking in a triangulation.* Int J Found Comput S, **13** (2): 181-199.

Edahiro M., Kokubo I. & Asano T. (1984) - *A new point-location algorithm and its practical efficiency: comparison with existing algorithms*. ACM T Graphic, **3** (2): 86-109.

Fekken G., Veldman A.E.P. & Buchner B. (1999) - *Simulation of green-water loading using the Navier-Stokes equations*. Proc. 7th Int. Conf. on Numerical Ship Hydrodynamics, 19-22 July, Nantes, France, 745-752.

Hirsch C. (1991, Ed.) - *Numerical computation of internal and external flows. Volume 1: fundamental of numerical discretization.* John Wiley and Sons Ltd, Chichester, United Kingdom.

Kirkpatrick D. (1983) - *Optimal search in planar subdivisions*. SIAM J Comput, **12** (1): 28-35.

Mandø M. & Rosendahl L. (2010) - *On the motion of non-spherical particles at high Reynolds number.* Powder Technol, **202**: 1-13. http://dx.doi:10.1016/j.powtec.2010.05.001

Maxey M.R. & Riley J.J. (1983) - *Equation of motion for a small rigid sphere in a nonuniform flow.* Phys Fluids, **26** (4): 883-889.

Mazzorana B., Hübl J., Zischg A. & Largiader A. (2011) - *Modelling woody material transport and deposition in alpine rivers.* Nat Hazards, **56** (2): 425-449. http://dx.doi:10.1007/s11069-009-9492-y

Meyer M., Barr A., Lee H. & Desbrun M. (2002) - *Generalized barycentric coordinates on irregular polygons.* J Graph Tools, **7** (1): 13-22.

Mücke E.P., Saias I. & Zhu B. (1999) - *Fast randomized point location without preprocessing in two-and three-dimensional Delaunay triangulations.* Comput Geom, **12** (1-2): 63-83.

Persi E., Petaccia G. & Sibilla S. (2018) - *Large wood transport modelling by a coupled Eulerian-Lagrangian approach.* Nat Hazards, **91**: 59-74.

Petaccia G., Soares-Frazão S., Savi F., Natale L. & Zech Y. (2010) - *Simplified versus detailed two-dimensional approaches to transient flow modeling in urban areas.* J Hydraul Eng-ASCE, **136** (4): 262-266. http://dx.doi:10.1061/(ASCE)HY.1943-7900.0000154

Petaccia G., Leporati F. & Torti E. (2016) - *OpenMP and CUDA simulations of Sella Zerbino Dam break on unstructured grids*. Computat Geosci, **20** (5): 1123-1132.

Preparata F.P. (1990) - *Planar point location revisited.* Int J Found Comput S, **1** (1): 71-86.

Ruiz-Villanueva V., Bladé Castellet E., Díez-Herrero A., Bodoque J.M. & Sánchez-Juny M. (2014a) - *Two-dimensional modelling of large wood transport during flash floods*. Earth Surf Proc Land, **39** (4): 438-449. http://dx.doi:10.1002/esp.3456

Ruiz-Villanueva V., Bladé E., Sánchez-Juny M., Marti-Cardona B., Díez-Herrero A. & Bodoque J.M. (2014b) - *Two-dimensional numerical modeling of wood transport*. J Hydroinform, **16** (5): 1077-1096.

Soares-Frazão S., Lhomme J., Guinot V. & Zech Y. (2008) - *Two-dimensional shallow-water model with porosity for urban flood modelling*. J Hydraul Res, **46** (1): 45-64.

Soukal R., Málková M., Vomácka T.& Kolingerová I. (2011) - *Hybrid walking point location algorithm.* Proc. 5th Int Conf. ADVCOMP, November 20-25, Lisbon, Portugal.

Stockstill R.L., Daly S.F. & Hopkins M.A. (2009) - *Modeling floating objects at river structures*. Journal Hydraul Eng-ASCE, **135** (5): 403-414. http://dx.doi:10.1061/(ASCE)0733-9429(2009)135:5(403)

Sukumar N. & Tabarraei A. (2004) - *Conforming polygonal finite elements.* Int J Numer Meth Eng, **61** (12): 2045-2066.

Toro E. (2009) - *Riemann solvers and numerical methods for fluid dynamics: a practical introduction.* Springer-Verlag Berlin Heidelberg.

Received April 2017 - Accepted November 2017